NOTES AND CORRESPONDENCE

Application of Aerosondes to Melt-Pond Observations over Arctic Sea Ice

JUN INOUE

Institute of Observational Research for Global Change, Japan Agency for Marine-Earth Science and Technology, Yokosuka, Japan

JUDITH A. CURRY

School of Earth and Atmospheric Sciences, Georgia Institute of Technology, Atlanta, Georgia

JAMES A. MASLANIK

Department of Aerospace Engineering Sciences, University of Colorado, Boulder, Colorado

ABSTRACT

Continuous observation of sea ice using a small robotic aircraft called the Aerosonde was made over the Arctic Ocean from Barrow, Alaska, on 20–21 July 2003. Over a region located 350 km off the coast of Barrow, images obtained from the aircraft were used to characterize the sea ice and to determine the fraction of melt ponds on both multiyear and first-year ice. Analysis of the data indicates that melt-pond fraction increased northward from 20% to 30% as the ice fraction increased. However, the fraction of ponded ice was over 30% in the multiyear ice zone while it was about 25% in the first-year ice zone. A comparison with a satellite microwave product showed that the ice concentration derived from the Advanced Microwave Scanning Radiometer for the Earth Observing System (AMSR-E) has a negative bias of 7% due to melt ponds. These analyses demonstrate the utility of recent advances in unmanned aerial vehicle (UAV) technology for monitoring and interpreting the spatial variations in the sea ice with melt ponds.

1. Introduction

In recent years, observations from satellite microwave sensors have revealed a new minimum in the Arctic ice extent recorded in September (Serreze et al. 2003; Stroeve et al. 2004; Comiso 2006). However, the operational passive microwave sensors have resolutions that are too coarse to distinguish open water from ponded ice. Hence, total ice concentrations determined from the satellite microwave sensors are not as accurate during the summer melt season as in winter (Cavalieri et al. 1984; Fetterer and Untersteiner 1998; Meier 2005). While satellite visible-band sensors have higher resolution, the persistent cloud cover over the ice pack

during summer (e.g., Inoue et al. 2005b) severely limits the utility of these sensors to observe melt ponds (e.g., Markus et al. 2003). Even with relatively high-resolution sensors such as Landsat, mixtures of ponds and pond-free ice are likely within the sensor field of view.

Although the melt ponds result in errors for estimating the ice concentration during the summer melt season, understanding the melt-pond evolution during summer is vital to understanding the sea ice–albedo feedback. Curry et al. (1995, 2001) argue that explicit treatment of melt ponds in climate models is needed for correct simulation of the sea ice albedo feedback. Evolution of melt ponds also modifies the amount of shortwave radiation into the open water through multiple reflections (Inoue et al. 2005a). Based on observations obtained (Perovich et al. 2002a) during the Surface Heat Budget of the Arctic (SHEBA) experiment (Uttal et al. 2002), detailed models of melt-pond evolution have been developed (e.g., Taylor and Feltham 2004;

Corresponding author address: Jun Inoue, Institute of Observational Research for Global Change, Japan Agency for Marine-Earth Science and Technology, 2-15 Natsushima-cho, Yokosuka 237-0061, Japan.
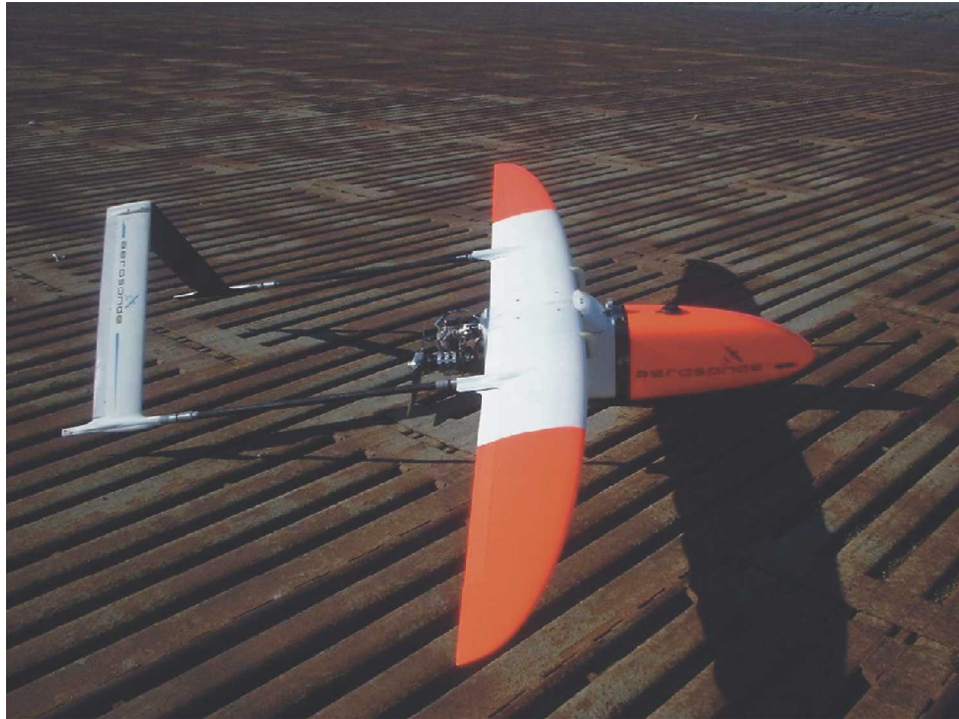E-mail: jun.inoue@jamstec.go.jp

FIG. 1. An Aerosonde after landing on the runway in Barrow.

Lüthje et al. 2006) that demonstrate the complexity of the summertime surface ablation of sea ice and the importance of melt ponds in this process.

Observations of melt ponds are challenging owing to the logistical difficulties and expense of in situ observations (e.g., Uttal et al. 2002) and to expense and hazards associated with low-altitude aircraft flights in the Arctic (Curry et al. 2004). During SHEBA, observations of pond and lead coverage were made on spatial ranges ranging from meters to order of 100 km using aircraft and in situ measurements (Tschudi et al. 2001; Perovich et al. 2002a,b).

To aid the interpretation of satellite imagery and to improve the treatment of melt ponds in sea ice models, increased observations are needed on pond characteristics on different ice types. To verify melt-pond distribution and error sources previously described in the literature, we demonstrate the utility of a new technology for observing melt ponds: a small unmanned aerial vehicle (UAV) equipped with a digital camera.

2. Identification of surface features

a. The Aerosonde system

The Aerosonde (Holland et al. 1992) is a small robotic aircraft that has a wing span of 2.9 m, weighs approximately 15 kg, and has a total payload capacity of 7 kg, which includes fuel plus instruments (Fig. 1). As for meteorological instrumentation, a thermodynamic and wind-observing capacity is standard on all Aerosondes. The Aerosonde flies with a mean speed of about 25 m s^{-1} and has an altitude range of between 100 and 7000 m. The small size of the Aerosonde allows it to be extremely fuel efficient so that flight durations can easily exceed 20 h with a range exceeding 3000 km. Iridium satellite communications are vital, enabling long-range flights of the aircraft. Aerosondes have been making observations in the Beaufort/Chukchi Seas, based from Barrow, Alaska, since 2000 (Holland et al. 2001; Maslanik et al. 2002; Curry et al. 2004; Inoue and Curry 2004).

In July 2003, the Beaufort Sea was characterized by warm air advection from Alaska associated with a low pressure system (Stroeve et al. 2004). An Aerosonde was launched at 1620 UTC 20 July 2003 and flew for 13 h. The flight pattern consisted of nearly level flight at altitude averaging 200 m with range between 160 and 220 m (Fig. 2).

During the day, the Aerosonde continuously monitored the ocean surface in the Beaufort Sea off the coast of Barrow, Alaska, using a digital camera (Olympus C3030). The Olympus 3030 was operated at a resolution of 2048 × 1536, with a focal length of 0.0065 m and field of view of 57.69°. Images were taken once per
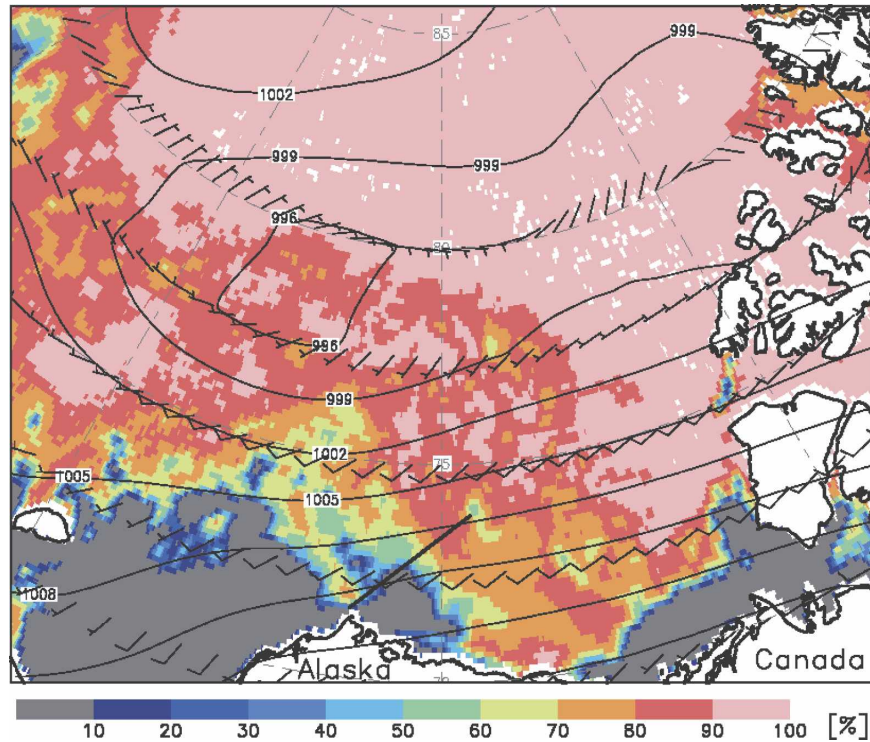
FIG. 2. AMSR-E derived ice concentration (%; shade), National Centers for Environmental Prediction–National Center for Atmospheric Research (NCEP–NCAR) sea level pressure (hPa; contour) and wind on 20 Jul 2003, respectively. Flight course is also denoted by a thick solid line.

30 s during the period of level flight. Each image covers an area of about 220 m × 169 m, yielding a resolution of 0.08 m per pixel at the 200-m altitude. A total of 470 images were collected and analyzed for this study. Figure 3 shows sample images of the sea ice surface taken by the aircraft. Basic meteorological parameters (air pressure, air temperature, humidity, and winds) were also observed simultaneously.

b. Processing of sea ice images

To assess the ice conditions quantitatively, the aerial photographs were processed using a free software package [GNU Image Manipulation Program (GIMP)] for personal computer–based image analysis. The program reads each image that contains the red, green, and blue digital values for each pixel. The partitioning of the images into the snow-covered and bare ice (A_i), ponded ice (A_p), and open water (A_w) was done by manually selecting red–green–blue (RGB) color thresholds based on color-distribution histograms and on the image itself. Selecting thresholds for each image compensates for changing surface and sky conditions during the flights. Each image was partitioned into three surface categories based on the following characteristics: 1) the

pond reflectance is greater in the blue portion of the spectrum than in the red, compared to the relatively flat spectral signature of the surrounding ice, and 2) the reflectance of open water is lower than that of first-year and multiyear ice, and its flat spectral return to distinguish it from the ponds. Thus, threshold levels for each surface category in each image were independently determined.

In this study, the ice concentration is defined as the sum of A_i and A_p. Once the fractional area per image of each feature type was calculated, results were normalized to total 100%. We neglected 7% of images that could not be processed because of poor contrast due to low clouds or fog.

Pondlike features were present at the edges of some regions of open water. These features typically resulted from lateral melting and edge erosion. In the fractional area analysis, these features are characterized as melt ponds because their optical properties are similar, and their effects on ice melt should also be similar to ponds on ice. Melt ponds that melted through appeared black (i.e., melt holes) and were optically similar to leads due to the same RGB distributions, and so were recorded as open water. These melted-through ponds are essentially equivalent to leads in physical terms, so treating
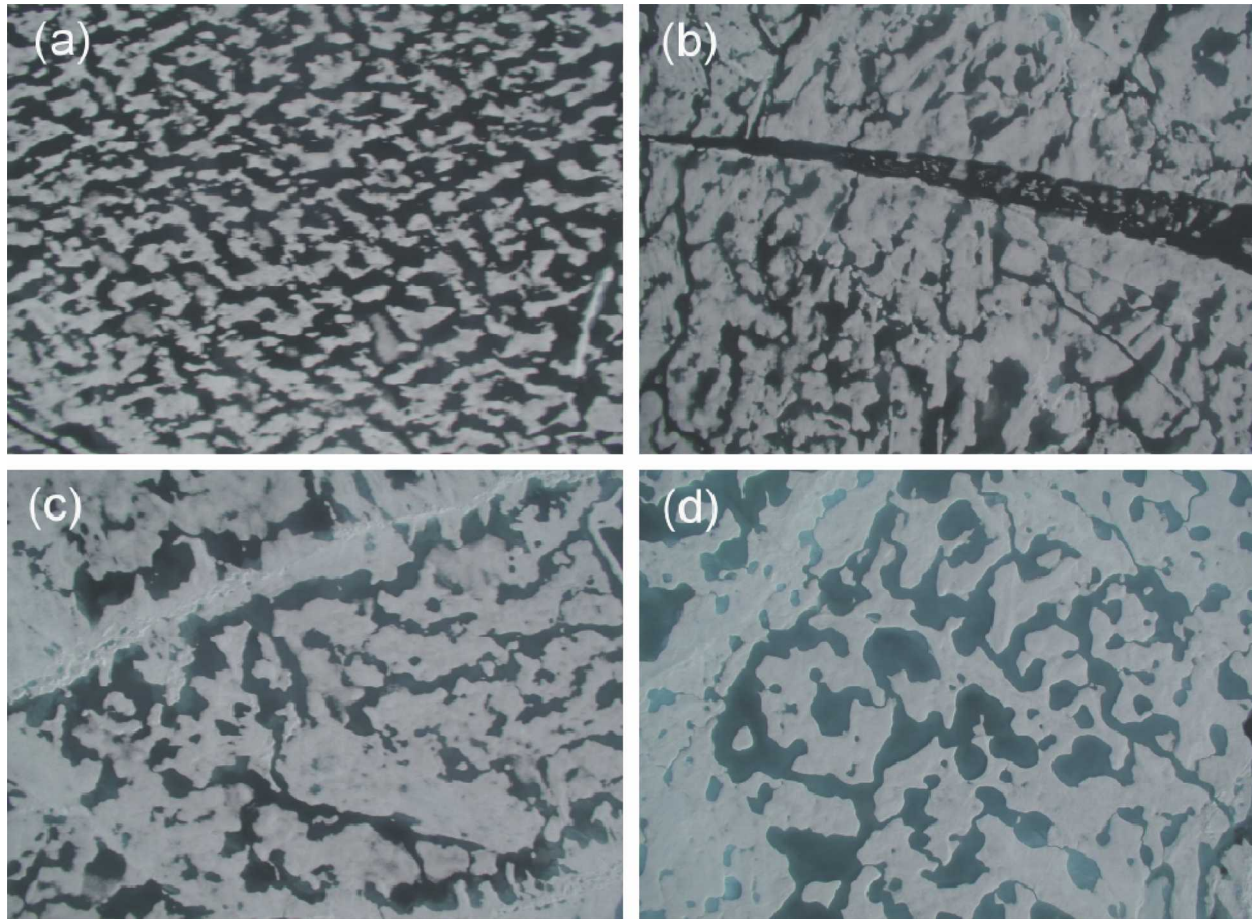
FIG. 3. Examples of sea ice images at (a) 72.8°, (b) 73.1°, (c) 73.4°, and (d) 73.7°N. The frame size is about 220 m × 169 m at 200-m altitude.

them as open water rather than ponds in the classification algorithm is warranted.

Because thresholds (over the digital number from 0 to 255) to partition the images into three surface categories are derived manually, there is uncertainty resulting from small changes in threshold values. Here, to estimate the error due to this effect, A_p is estimated by changing the thresholds with ±10 as probable perturbations. To make a choice at random, 10 images were selected between 72.8° and 73.7°N (once per 0.1°N). The selected images and their A_p are shown in Fig. 4; A_p varied from place to place, while their errors ranged between ±1.4% and ±5.0%. On the average, the error due to the change in thresholds was ±3.2%.

3. Melt-pond distribution

a. General features

Generally, multiyear ice can be distinguished from first-year ice due to the characteristic shape and color of melt ponds. Ponds on multiyear ice are usually more

well defined, sinuous, and cover a smaller portion of the ice surface than is the case for first-year ice. A seemingly random pattern of ponds are observed on multiyear ice, while on first-year ice the ponds tend to align their major axis with melting sastrugi. Whereas ponds on first-year ice are various shades of gray depending on pond depth, multiyear ice ponds are typically green to blue in color due to the underlying ice conditions. Other factors visible in aerial photographs, such as floe shape and surface topography, are also distinctive. From the viewpoint of these morphological properties of melt ponds, our long-distance observation presumably covers both first-year and multiyear ice areas and their transitional zone. Although all images were taken on the same day, our observations imply that the temporal evolution of ponds is apparent as described in Perovich et al. (2002b): water collects in patches on the ice surface (multiyear ice: Figs. 3c,d), and then ponds, continues to spread, and become ubiquitous (Fig. 3b). As the ponds spread, they connected into large, complex networks (e.g., first-year ice: Fig. 3a; multiyear ice:
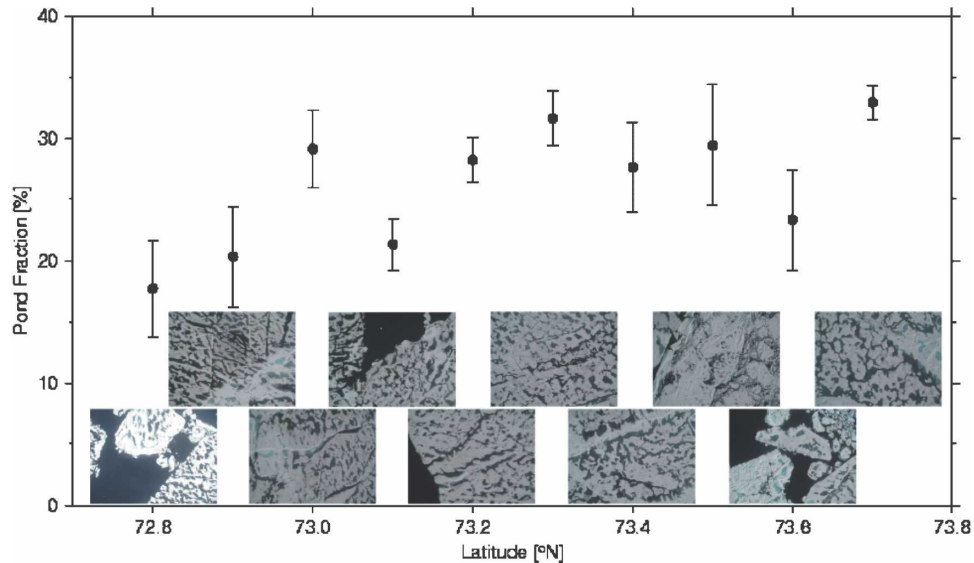
FIG. 4. Pond fraction (A_p) between 72.8° and 73.7°N. Error bars denote the range when the threshold values to decide A_p are varied ±10. Corresponding images to A_p are shown at bottom.

Fig. 3d) with pond shapes and arrangements differing considerably between first-year and multiyear ice. These characteristics reflect the relatively flat surface typical of first-year ice versus the combination of hummocks and melt ponds found of multiyear ice.

Figure 5 shows the latitudinal fractional distributions of water (A_w), melt pond (A_p), and ice (A_i). Open water located around 72.3°N is also seen in a satellite image (Fig. 2). However, the A_i increases sharply from 72.5°N northward; A_i and A_p gradually increase northward from 50% to 70% and 20% to 30%, respectively, resulting in the decrease of the air temperature from 13° to 2°C at the 200-m altitude partly due to downward sensible heat flux induced by the offshore wind (Fig. 2).

For comparison, melt-pond areal fraction analyzed using aircraft video images varies between 25% and 34% in July during SHEBA (Tschudi et al. 2001). Fetterer and Untersteiner (1998) also reported maximum pond fractions of 40%–50% on flat first-year ice and 30% on deformed multiyear ice during midsummer by using the visible satellite dataset during Polar Exchange at the Sea Surface 1995 (POLES'95). Therefore, the date of our observation may be close to the period with maximum pond coverage.

b. Comparison with a satellite microwave sensor

The red line in Fig. 5 shows the ice concentration derived from satellite microwave observations from the Advanced Microwave Scanning Radiometer for the Earth Observing System (AMSR-E) using the bootstrap algorithm at the closest grid point where the air-craft observed the sea ice. This algorithm has the lowest error standard deviation of estimating ice concentration during summer (Meier 2005). To compare this with observed A_i and A_p, aerial mean data fitted to the satellite resolution (12.5 km) are also superimposed by dashed ($A_i + A_p$) and dotted (A_i) lines in Fig. 5. Generally, the horizontal variability of ice concentration is the same for both the Aerosonde and AMSR-E observations, for example, the coastal moderate ice cover, wide open water area around 72.3°N, and highly ice-covered area in the northernmost area. However, it is clear that the satellite-derived ice concentration is lower than the observed ice concentration ($A_i + A_p$), and larger than A_i. The discrepancy between the satellite and Aerosonde observations implies that the melt ponds are a source of errors in the ice concentration determination using microwave data, although the magnitude of the effects remains uncertain (e.g., Fetterer and Untersteiner 1998).

Figure 6 shows the scatterplots of observed and satellite-derived ice concentrations. Closed and open circles are for $A_i + A_p$ and A_i, respectively. The satellite underestimates the ice concentration 7.0% ± 4.8% on the average. This tendency is similar to the summertime ice concentration derived from the Special Sensor Microwave Imager (SSM/I) by the bootstrap algorithm relative to the Advanced Very High Resolution Radiometer (AVHRR) product by channel 2 with 6.1% ± 14.6% (Meier 2005). As for visible sensors, a comparison of ice concentration between video and Landsat images yields an rms error of 8.9% with a negligible bias (Markus et al. 2003). Although the difference in
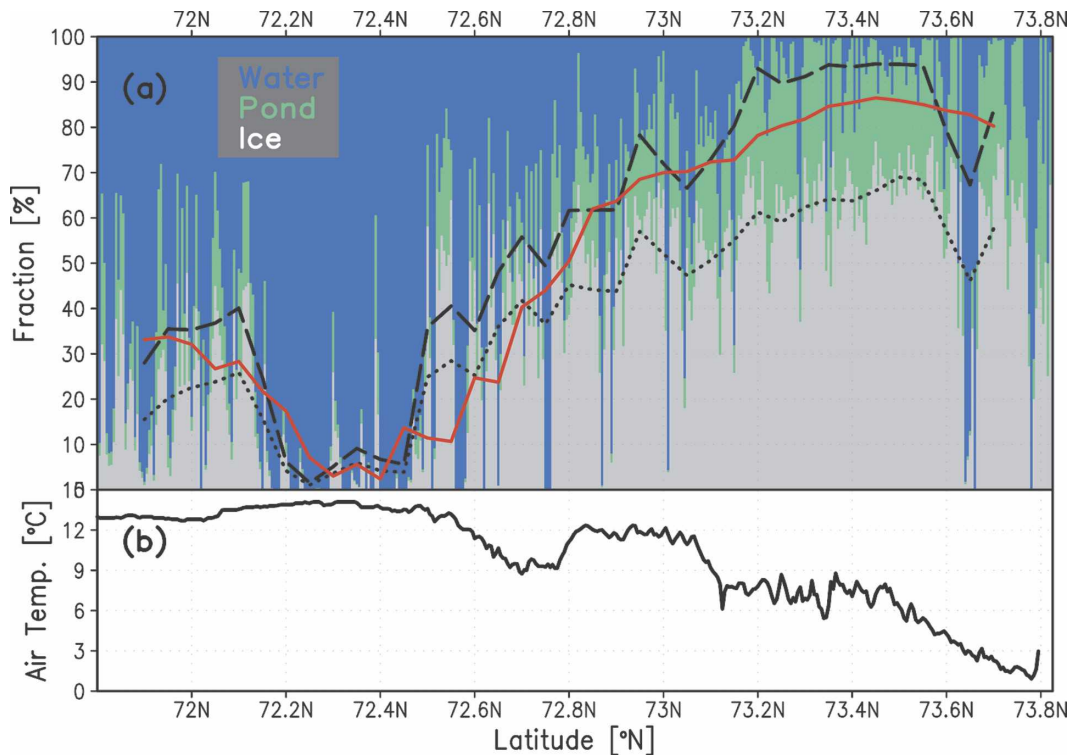
FIG. 5. (a) Fraction of water (A_w), pond (A_p), and ice (A_i) derived from image analyses. Red line shows the AMSR-E derived ice concentration. Averaged fractions of $A_i + A_p$ and A_i fitted the resolution of satellite data are also superimposed by long-dashed and dotted lines, respectively. (b) Air temperature observed at 200 m.

the spatial resolution might be a source of rms errors for each comparison, the bias arising from ice concentration derived from microwave sensors is presumably correct.
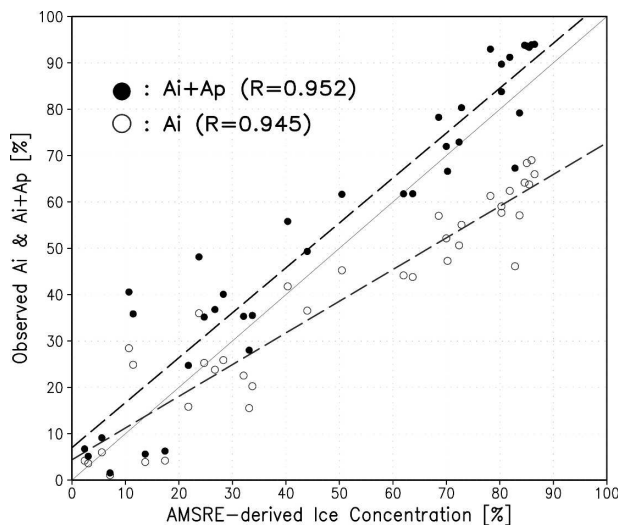

FIG. 6. Scatterplots and regression lines between observed and satellite-derived ice concentrations. Closed and open circles are for $A_i + A_p$ and A_i, respectively. The parameter R is the correlation coefficient.

c. Latitudinal evolution of melt ponds

It is known that the difference in roughness of ice surface causes the difference in pond properties (e.g., Yackel et al. 2000). To adjust the pond fraction to account for changes due to variations in ice concentration, the fraction of the ice that is ponded [$A_p^* = A_p/(A_i + A_p)$] is plotted in Fig. 7. In the region with high ice concentration (>50%), A_p^* is approximately 30%, while in the region with low ice concentration (<50%) at lower latitude (<72°N), A_p^* is larger than 35% with large standard deviations (±10%). Looking at A_p^* within the high ice-covered area (>72.6°N) more carefully, A_p^* decreases southward from 30% to 25%. Although studies indicate that general pond fractions on first-year ice are greater than those on multiyear ice (Fetterer and Untersteiner 1998; Naggar et al. 1998), the decrease in A_p^* is also reported due to enhanced drainage resulting from increased ice permeability (Perovich et al. 2002b).

Using the sea ice images obtained by an aircraft in July during SHEBA, Tschudi et al. (2001) showed that the ratio of melt holes to the total pond fraction increased from 21% to 31% as the melt season advanced. In their analysis, the total pond fraction including holes also increased from 25% to 34%, suggesting that the
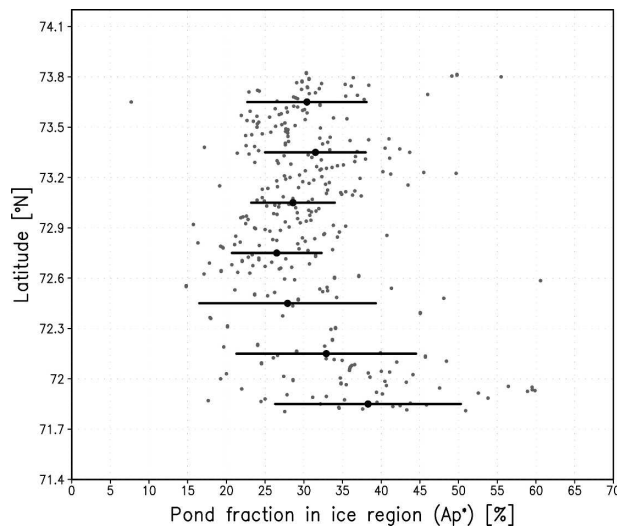
FIG. 7. Latitudinal distributions of pond fraction in ice region $[A_p^* = A_p/(A_i + A_p)]$. Averaged values for 0.3° bins and their one standard deviation are shown by black dots and horizontal lines.

to provide aerial coverage over much of the Beaufort and Chukchi Seas, coincident with satellite overpasses. This allows observations over a range of ice types, including shorefast ice, the marginal ice zone, the first-year seasonal ice cover, and multiyear ice. The ability of Aerosondes to remain airborne for over 20 h also allows mapping of the temporal evolution of ponds, and the aircraft's capability to operate autonomously at a large range of altitudes is valuable for the study of the effects of imaging spatial resolution on algorithm accuracy and the representativeness of spatially averaged albedo. Relative to piloted aircraft, costs and logistics requirements for small UAVs are typically less, the UAVs can operate in conditions not suitable for manned aircraft, and personnel are not put at risk.

melt-hole fraction should increase from 5% to 10%. Because melt holes tend to break out at thinner ice area, relatively high melt-hole fraction seems to appear in the relatively low-latitude region (e.g., at 72.8°N; Fig. 3a), where first-year ice dominantly exists. Therefore, the southward decrease in A_p^* might come from the evolution of melt holes, which are classified as open water area in this study.

4. Conclusions

The high temporal and spatial resolution of the Aerosonde observations, and its capability of flying beneath clouds, has demonstrated the variability of sea ice with melt ponds in the Arctic Ocean. Since satellite validation efforts often rely on images collected during clear skies, the ability to acquire surface imagery and other information below cloud cover can help remove potential biases in such validation efforts. This may be particularly important for validation of passive microwave product, since while the effects of cloud cover are considered minimal at microwave frequencies, atmospheric conditions can affect microwave-derived ice concentration and ice type algorithms (e.g., Maslanik 1992). The Aerosonde technology has the potential to improve the remote sensing of sea ice during the summer melt season and also to contribute to our ability to simulate the summertime melting of sea ice. For example, the long range (1500 km or greater) allows operations from a single location such as Barrow, Alaska,

REFERENCES

Cavalieri, D., P. Gloersen, and W. J. Campbell, 1984: Determination of sea ice parameters with the Nimbus 7 SMMR. *J. Geophys. Res.,* **89,** 5355–5369.

Comiso, J., 2006: Arctic warming signals from satellite observations. *Weather,* **61,** 70–76.

Curry, J. A., J. Schramm, and E. E. Ebert, 1995: On the sea ice albedo climate feedback mechanism. *J. Climate,* **8,** 240–247.

——, J. L. Schramm, D. Perovich, and J. O. Pinto, 2001: Application of SHEBA/FIRE data to evaluation of sea ice surface albedo parameterizations. *J. Geophys. Res.,* **106,** 15 345–15 356.

——, J. Maslanik, G. J. Holland, and J. O. Pinto, 2004: Applications of aerosondes in the Arctic. *Bull. Amer. Meteor. Soc.,* **85,** 1855–1861.

Fetterer, F., and N. Untersteiner, 1998: Observations of melt ponds on Artic sea ice. *J. Geophys. Res.,* **103,** 24 821–24 835.

Holland, G. J., T. McGeer, and H. Youngren, 1992: Autonomous aerosondes for economical atmospheric soundings anywhere on the globe. *Bull. Amer. Meteor. Soc.,* **73,** 1987–1998.

——, and Coauthors, 2001: The Aerosonde robotic aircraft: A new paradigm for environmental observations. *Bull. Amer. Meteor. Soc.,* **82,** 889–901.

Inoue, J., and J. A. Curry, 2004: Application of aerosondes to high-resolution observations of sea surface temperature over Barrow Canyon. *Geophys. Res. Lett.,* **31,** L14312, doi:10.1029/2004GL020336.

——, T. Kikuchi, D. K. Perovich, and J. Morison, 2005a: A drop in mid-summer shortwave radiation induced by changes ice-

surface condition in the central Arctic. *Geophys. Res. Lett.,* **32,** L13603, doi:10.1029/2005GL023170.

——, B. Kosović, and J. A. Curry, 2005b: Evolution of a storm-driven cloudy boundary layer in the Arctic. *Bound.-Layer Meteor.,* **117,** 213–230.

Lüthje, M., D. L. Feltham, P. D. Taylor, and M. G. Worster, 2006: Modeling the summertime evolution of sea-ice melt ponds. *J. Geophys. Res.,* **111,** C02001, doi:10.1029/2004JC002818.

Markus, T., D. J. Cavalieri, M. A. Tschudi, and A. Ivanoff, 2003: Comparison of aerial video and Landsat 7 data over ponded sea ice. *Remote Sens. Environ.,* **86,** 458–469.

Maslanik, J. A., 1992: Effects of weather on the retrieval of sea ice concentration and ice type from passive microwave data. *Int. J. Remote Sens.,* **13,** 37–54.

——, J. A. Curry, S. Drobot, and G. Holland, 2002: Observations of sea ice using a low-cost unpiloted aerial vehicle. *Proc. 16th IAHR Int. Symp. on Sea Ice,* Vol. 3, Dunedin, New Zealand, International Association of Hydraulic Engineering and Research, 283–287.

Meier, W. N., 2005: Comparison of passive microwave ice concentration algorithm retrievals with AVHRR imagery in Arctic peripheral seas. *IEEE Trans. Geosci. Remote Sens.,* **43,** 1324–1337.

Naggar, S. El, C. Garrity, and R. O. Ramseier, 1998: The modelling of sea ice melt-water ponds for the high Arctic using an airborne line scan camera, and applied to the satellite Special Sensor Microwave/Imager (SSM/I). *Int. J. Remote Sens.,* **19,** 2373–2394.

Perovich, D. K., T. C. Grenfell, B. Light, and P. V. Hobbs, 2002a: Seasonal evolution of the albedo of multiyear Arctic sea ice. *J. Geophys. Res.,* **107,** 8044, doi:10.1029/2000JC000438.

——, W. B. Tucker III, and K. A. Ligett, 2002b: Aerial observations of the evolution of ice surface conditions during summer. *J. Geophys. Res.,* **107,** 8048, doi:10.1029/2000JC000449.

Serreze, M. C., and Coauthors, 2003: A record minimum arctic sea ice extent and area in 2002. *Geophys. Res. Lett.,* **30,** 1110, doi:10.1029/2002GL016406.

Stroeve, J., M. C. Serreze, F. Fetterer, T. Arbetter, W. Meier, J. Maslanik, and K. Knowles, 2004: Tracking the Arctic's shrinking ice cover: Another extreme September minimum in 2004. *Geophys. Res. Lett.,* **32,** L04501, doi:10.1029/2004GL021810.

Taylor, P. D., and D. L. Feltham, 2004: A model of melt pond evolution on sea ice. *J. Geophys. Res.,* **109,** C12007, doi:10.1029/2004JC002361.

Tschudi, M. A., J. A. Curry, and J. A. Maslanik, 2001: Airborne observations of summertime surface features and their effect on surface albedo during FIRE/SHEBA. *J. Geophys. Res.,* **106,** 15 335–15 344.

Uttal, T., and Coauthors, 2002: Surface Heat Budget of the Arctic Ocean. *Bull. Amer. Meteor. Soc.,* **83,** 225–275.

Yackel, J. J., D. G. Barber, and J. M. Hanesiak, 2000: Melt ponds on sea ice in the Canadian Archipelago. 1. Variability in morphological and radiative properties. *J. Geophys. Res.,* **105,** 22 049–22 060.